

See discussions, stats, and author profiles for this publication at: <https://www.researchgate.net/publication/263251368>

Poly(hydroxyalkanoate) Elastomers and Their Graphene Nanocomposite

ARTICLE *in* MACROMOLECULES · JUNE 2014

Impact Factor: 5.8 · DOI: 10.1021/ma500022x

CITATIONS

5

READS

98

3 AUTHORS, INCLUDING:



Ahmed A. Abdala

Qatar Environment and Energy Research Ins...

56 PUBLICATIONS 5,108 CITATIONS

SEE PROFILE

Poly(hydroxyalkanoate) Elastomers and Their Graphene Nanocomposites^{||}

John S. F. Barrett,^{†,‡} Ahmed A. Abdala,^{*,§,⊥} and Friedrich Srienc^{*,†,‡}

[†]Department of Chemical Engineering and Materials Science, University of Minnesota, Minneapolis, Minnesota 55455, United States

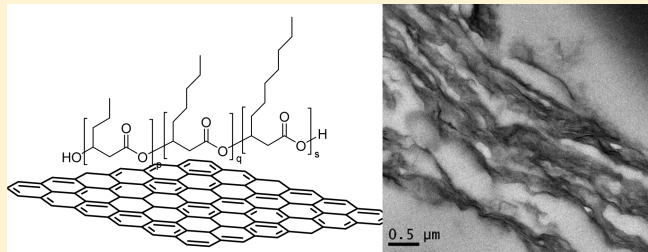
[‡]Biotechnology Institute, University of Minnesota, St. Paul, Minnesota 55108, United States

[§]Department of Chemical Engineering, the Petroleum Institute, Abu Dhabi, United Arab Emirates

[⊥]Department of Chemical Engineering and Petroleum Refining, Faculty of Petroleum and Mining Engineering, Suez University, Suez, Egypt

Supporting Information

ABSTRACT: Medium-chain-length poly(hydroxyalkanoate)s (PHA_{mcl}) are biodegradable and renewable biopolymers with elastomeric qualities. Here we report on the preparation and characterization of composite materials using thermally reduced graphene (TRG) nanoparticles as filler with three PHA_{mcl} polymers. The matrices vary with respect to chain packing length, capacity for noncovalent bonding with the TRG surface, and the presence of covalent cross-linking. Results show that the addition of up to 2.5 vol % TRG to PHA_{mcl} increases the melting temperature by 1–3 °C, the modulus by 200–590%, and the electrical conductivity by >7 orders of magnitude. Additionally, we use rheology and microscopy to characterize the composites. We discuss our results in light of polymer entanglement theory and the effects of polymer structure, filler loading volume, and the role of graphene-polymer interfacial forces. We extend our discussion by comparing the modulus enhancements of PHA_{mcl} composites to those reported in other studies in which layered carbon nanofillers are combined with structurally related biopolymers including: polylactide, polylactide-*co*-polyglycolide, polycaprolactone, and two other PHA copolymers.



INTRODUCTION

Poly(3-(*R*)-hydroxyalkanoates) (PHA) are a class of polymeric materials produced naturally by a variety of environmental microorganisms as a means of carbon and energy storage during times of nutrient excess.¹ Polymer synthesis occurs via the action of a synthase enzyme and results in the accumulation of small insoluble inclusions within the cell. Purification of PHA from residual cell biomass produces a plastic material with physical and mechanical properties similar to those of petroleum-derived polymers. The desirability of PHA is due to its characteristics of rapid biodegradation,¹ biocompatibility for use in medical applications,² and synthesis from a variety of renewable feedstocks including sugars,³ plant oils,⁴ industrial and municipal waste streams,⁵ and carbon dioxide.⁶ Polyhydroxybutyrate (PHB, C₄), the most common form of PHA, has a Young's modulus of 3.5–4 GPa, <5% elongation at break, and a melting temperature of 175–180 °C.⁷ Medium-chain-length poly(hydroxyalkanoate)s (PHA_{mcl}, C₆–C₁₄), which are more elastomeric, have a Young's modulus of 0.003–0.07 GPa, up to 500% elongation at break, and a melting temperature of 45–60 °C.^{8,9} Despite the useful characteristics of these basic forms of PHA, their continued proliferation into new applications requires the development of a more diverse range of physical and mechanical properties.

One commonly employed technique for enhancing the physical and mechanical properties of polymers is via the formation of composite materials by dispersion of fillers into the polymer matrix. Moreover, a growing trend has been in the use of nanosized filler materials, i.e., nanocomposites. Because of their small size, nanofillers provide a large surface area for molecular contact with the polymer chains at a minimal loading. A few PHB composites have already been studied with nanofillers including: wood flour,¹⁰ clay,¹¹ layered silicate,¹² and carbon nanotubes.^{13,14} The addition of these nanofillers resulted in changes in the thermal, mechanical, and crystallization properties of PHB.

Among nanofiller materials, carbon allotropes, which include exfoliated graphite,¹⁵ carbon nanotubes,¹⁶ and graphene,¹⁷ have received additional attention because of their exceptional strength, low weight, and capacity for electrical conductivity. Graphene, the nanofiller used in this study, is an atomic-thick sheet of sp²-hybridized carbon atoms. With measured Young's modulus and ultimate strength of 1 TPa and 130 GPa, respectively, graphene is the stiffest and strongest material ever

Received: January 4, 2014

Revised: May 11, 2014

measured.¹⁸ The theoretical surface area of graphene¹⁹ is estimated to be 2630 m²/g. The addition of graphene to various polymers has been shown to enhance their resistance to thermal degradation, improve mechanical properties, increase electrical conductivity, and lower gas permeability.²⁰ Moreover, theoretical and experimental results indicate that the modulus enhancement with graphene addition is more pronounced with low-modulus, elastomeric polymers than with high-modulus, glassy polymers.²⁰ Therefore, the addition of graphene has a significant potential for creating a range of useful functionalities in a class of polymers that is highly valued for its eco-friendly and biocompatible qualities.

Understanding the way by which a nanofiller affects the viscoelastic properties of dense polymer systems is based on the theory of polymer entanglements. These entanglements can form between neighboring polymer chains^{21–23} as well as between the polymer and the nanofiller.^{24–28} Adding nanofiller to a polymer matrix alters its viscoelastic behavior due to the formation of additional entanglements between the particles and the polymer chains, thereby enhancing the stiffness of the polymer matrix. While attractive intermolecular forces between the matrix and filler do contribute to the viscoelastic behavior of nanocomposites, size, shape and aspect ratio of the nanofillers also have significant influence on reinforcing effects,^{26,29,30} and the existence of molecular attraction between the matrix and filler is not required for reinforcement to occur.^{28,31} The prevalent theory of this phenomenon is that noninteracting nanoparticles block and confine the primitive paths of reptating chains, creating entanglements purely based on physical interactions.^{26–28}

When interfacial forces between graphene sheets and the polymer matrix are significantly attractive, additional entanglements can originate at the interface.²⁵ Transmission of stress between the matrix and the graphene surface can occur via π - π stacking, cation- π , or van der Waals interactions with available sp² networks.³² Graphite oxide (GO), an alternate form of graphene, contains additional moieties such as epoxide, carbonyl, and hydroxyl groups on the surface that permit the formation of hydrogen bonds. GO can be reduced chemically or thermally to produce reduced graphene with much lower oxygen content than GO. In this study, we use thermally reduced graphene (TRG) which is synthesized by rapid heating of GO that leads to simultaneous reduction and exfoliation of the GO layers. The C:O ratio of TRG is 10:1 compared to 2:1 for GO³³ While hydrogen bonding can occur between TRG and the polymer matrix, it can also occur between multiple sheets of TRG, thereby leading to particle aggregation and poor dispersion. Modification of reduced graphene by incorporating other chemical moieties on its surface can also be used to promote interfacial attraction with a specific matrix.²⁰

Herein, we report on the preparation of composite materials by incorporating TRG into three, unique PHA_{mcl} copolymers: nominally, they are PHO (polhydroxyoctanoate, C₈), PHD (polhydroxydecanoate, C₁₀), and PHOe (polyhydroxyoctenoate, C₈). The copolymers vary in their composition of C₆, C₈, and C₁₀ monomers. While all polymers contain a majority of C₈ monomers, PHD contains a significant fraction of C₁₀ monomers and is predicted to have a greater packing length based on its cross-section, which is wider than that of PHO. Thus, PHD should be less likely to participate in polymer entanglements. Moreover, the longer aliphatic appendages of PHD can shield noncovalent bonding with the polyester backbone. PHOe is very similar to PHO with the exception that

PHOe contains a small fraction of C₈ monomers with an unsaturated carbon at the terminal position. Thus, PHOe is capable of forming a network structure via covalent cross-linking. We discuss the effectiveness of graphene reinforcement in each matrix in the theoretical context of polymer entanglements and the ability of each polymer to engage in noncovalent interactions with the oxygenated TRG surface. Finally, we compare our results to other studies in the literature that combine layered carbon nanofillers with similar biodegradable polyesters. Figure 8 depicts the chemical structures of the different PHA_{mcl} matrices along with related polyoxoesters.

MATERIALS AND METHODS

PHA Synthesis. Synthesis of the various PHA_{mcl} copolymers was performed by a method similar to that used by Lageveen et al.³⁴ Briefly, the polymers were produced by fed-batch biosynthesis using the wild-type organism *Pseudomonas oleovorans* in minimal media with specific alkanes as the sole carbon source. Octane, decane, and octene were used to synthesize polyhydroxyoctanoate (PHO) polyhydroxydecanoate (PHD) and polyhydroxyoctenoate (PHOe) respectively. More specifically, the PHOe copolymer was synthesized via repeated cycles between octane and 1-octene. Previous studies on the synthesis of PHA copolymers suggested that repeated cycling between different carbon sources produces a mixture of the two corresponding polymer types with some fraction of the polymer chains expected to be di- and triblock-copolymers.^{35,36} Additional details of the biosynthesis are available in the Supporting Information.

Following polymer biosynthesis cells were harvested via centrifugation at 10 000 rpm for 20 min. The resulting cell pellet was flash frozen in liquid nitrogen and lyophilized overnight to remove residual moisture. Polymer material was extracted from the dried cells into 1-L of boiling chloroform for 16 h using a Soxhlet apparatus. The extract was concentrated by evaporation to 100 mL before precipitation in excess methanol, 8:1 (v/v). The purified polymer was dried in air to remove excess solvent.

PHA Characterization. Purified PHAs were analyzed via gas chromatography fitted with a flame ionization detector (GC-17A, Shimadzu) using a DB-WAX column (ID 0.32 mm, 0.5 μ m film thickness) (Agilent Technologies). Prior to analysis, polyhydroxyalkanoic acids were converted to 3-hydroxyalkanoic propyl esters by the method of propanolysis.³⁷ Quantitative determination of different PHAs was made by comparison to standards synthesized from purified 3-hydroxyalkanoic acids (Sigma).

Polymer molecular weights were determined by gel permeation chromatography (PL GPC 220 high temperature chromatograph, Polymer Laboratories) using 3, PL-gel 10 μ m mixed B columns in series. TCB (1,2,4-trichlorobenzene) was used as the mobile phase, and the column was operated at 160 °C. Calibration of the instrument was performed using polystyrene standards, and molecular weights are reported in polystyrene equivalents.

Graphene Synthesis. Thermally reduced graphene (TRG) was produced following the thermal exfoliation method.^{33,38} In this method, graphite was first oxidized using Staudenmaier method³⁹ as follows: 5 g of graphite was placed in an ice-chilled flask containing a mixture of 90 mL of H₂SO₄ and 45 mL of HNO₃. Potassium chloride, 55 g, was slowly added to the cold reaction mixture. After 96 h, the reaction was quenched by combining the mixture with 4 L of water. The resulting graphite oxide (GO) was washed once in 5% HCl followed by additional water washes to remove the residual acid before drying overnight in a vacuum oven. TRG was produced by exfoliating the GO via rapid heating in a tube furnace (Barnstead Thermolyne) at 1000 °C under a flow of nitrogen for 30 s.

Graphene Characterization. Graphene was characterized by X-ray diffraction and transmission electron microscopy. Details of these characterization methods are provided in the Supporting Information.

PHA–Graphene Nanocomposite Preparation. First, 1 g of polymer was mixed with 20 mL of chloroform in a sealed tube and agitated using a vortex mixer. Periodic incubation of the mixture in an

Table 1. Chemical Composition and Molecular Weight of Purified Poly(hydroxyalkanoate)s

	molecular weight ^a		composition ^b (% wt)					
	M_w (10 ³ g/mol)	M_w/M_n	3HB	3HH	3HH _{6:1}	3HO	3HO _{8:1}	3HD
PHO	71	3.1	0.4	7.0	—	91.4	—	1.2
PHOe	54	2.3	—	4.2	<0.1	89.5	6.1	<0.1
PHD	57	2.6	0.4	6.4	—	61.5	—	31.7

^aWeight-average molecular weight (M_w); number-average molecular weight (M_n). ^b3HB (3-(R)-hydroxybutyrate), 3HH (3-(R)-hydroxyhexanoate), 3HH_{6:1} (3-(R)-hydroxyhexenoate), 3HO (3-(R)-hydroxyoctanoate), 3HO_{8:1} (3-(R)-hydroxyoctenoate), and 3HD (3-(R)-hydroxydecanoate).

80 °C water bath was used to promote dissolution. Second, graphene was dispersed in chloroform at a concentration of 0.5 mg/mL. To promote the dispersion of single graphene sheets, the mixture was sonicated for 6 min using a probe type sonicator (Misonix 3000) at a power density of 1.5–3 W/mL. The sonicator program consisted of 28 cycles of 15 s sonication followed by a 45 s rest period to dissipate heat. The graphene dispersion was then added to the polymer solution and stirred for 1 h. The nanocomposite solution was solvent-cast by transferring it into a Petri dish placed over a 55 °C hot plate with light stirring for ~1 h. Films were dried overnight to remove excess chloroform.

PHA–Graphene Nanocomposite Characterization. The non-oxidative thermal stability of the pure and composite samples was assessed using a simultaneous thermal analyzer (STA) (Netzsch STA 449 F1 Jupiter), which performs both thermal gravimetric analysis (TGA) and differential scanning calorimetry (DSC). The polymer nanocomposite sample (~10 mg) was placed in a ceramic crucible and heated from 25–600 °C at a heating rate of 20 °C/min under nitrogen flow.

The glass transition temperature (T_g), melting temperature (T_m), and heat of melting (ΔH_m) of the pure and composite samples were measured using differential scanning calorimetry (Netzsch 204 F1 Phoenix). The polymer nanocomposite sample (6–10 mg) was placed in crimped but unsealed aluminum pans and heated from –60 to +250 °C at a heating rate of 5 °C/min under nitrogen flow. All samples were aged for 72 h prior to testing.

Specimens for mechanical, rheological, and surface resistance measurements were prepared using a hot-press (Tetrahedron, MTP-10) at 100 °C and 1.0 MPa for 5 min to form a thin film (0.4–0.5 mm). Samples were aged at room temperature for >72 h prior to testing. Surface resistance measurements were obtained using an 11-point probe (Prostat Corp., PRF-914B probe with PRS-801 meter). For each sample, four readings were collected, two from each side of the film.

The rheological properties of the pure and composite samples were determined via dynamic oscillatory measurement (TA Instruments, AR2000ex) using an 8 mm parallel plate geometry. Strain and frequency sweeps were performed on 8 × 0.5 mm circular disks at 70 °C.

The mechanical properties of the pure and composite samples were measured using a dynamic mechanical analyzer (DMA) (TA Instruments, RSAIII). 50 × 5 × 0.5 mm specimens were tested at a strain rate of 5 mm/min.

The fracture surface of the pure and composite samples were examined using SEM (Philips FEI Quanta 200 SEM) operated at a high-vacuum mode.

Dispersion of graphene within the polymer matrix was analyzed with transmission electron microscopy (TEM) (JEOL, 1200 EXII). Thin sections of composite samples, 70–100 nm, for TEM characterization were prepared without resin embedding using an ultramicrotome (Leica EM UC6) at –80 °C. Samples were mounted on 200-mesh copper grids with carbon type-B coating (Ted Pella)

RESULTS AND DISCUSSION

Properties of Purified PHA. Poly(hydroxyalkanoate) (PHA) polymers were produced *in vivo* using the microorganism *Pseudomonas oleovorans* with different hydrocarbons as substrates. The composition of different polymer samples

can be controlled via the type of carbon substrate fed to the batch during biosynthesis, e.g., the metabolism of octane produces the monomer 3-(R)-hydroxyoctanoyl-CoA, and decane produces 3-(R)-hydroxydecanoyl-CoA. However, due to the cyclical nature of the β-oxidation pathway, which degrades these molecules, the metabolism of a single substrate produces a random copolymer consisting of related monomers differing by –2n carbons, where n is number of β-oxidation cycles.⁷ A detailed description and schematic of this process are included in the Supporting Information.

Nominally, PHO (polyhydroxyoctanoate), PHOe (polyhydroxyoctenoate), and PHD (polyhydroxydecanoate) designate copolymer materials that contain full-length monomers as well as shorter monomers created by β-oxidation. PHO and PHD were synthesized from octane and decane, respectively. PHOe was synthesized from cyclical additions of octane and octene and so contains both saturated and unsaturated monomers along the polymer chain.⁴⁰ Given the cyclical nature in which octane and octene feeds were administered, we expect that the purified polymer may contain some block copolymer molecules^{35,36} composed of distinct domains enriched in polyhydroxyoctene. The presence of double bonds along the polymer backbone of PHOe permits the formation of chemical cross-links between chains. In a previous report, researchers produced similar poly(hydroxyalkanoate) polymers synthesized from octane and octene and subjected them to varying intensities of electron-beam radiation to promote cross-linking.⁴⁰ While PHOe used in this study was never subjected to concentrated radiation, its exposure to environmental, ultraviolet radiation over a 1-year period likely contributed to the formation of a small degree of cross-linking. Furthermore, it is possible that additional cross-linking occurred under the elevated temperature (100 °C) used for melt-pressing composite specimens. Table 1 provides the composition and molecular weight for the pure polymers. As a caveat to the molecular weight data, we remind the reader that all values are reported as polystyrene equivalents, which does not account for the fact that given equivalent molecular weights, polymers with a larger cross-section and thus a larger hydrodynamic volume elute faster during size-exclusion chromatography. Between PHO and PHOe, we expect little difference in the hydrodynamic volume based on their similar monomer composition. PHD, we anticipate, may have a larger hydrodynamic volume due to its longer aliphatic appendages. Thus, the comparison between PHD and PHO according to polystyrene equivalents may actually underestimate the difference in molecular weight. Furthermore, Nerkar et al. have reported that for GPC measurements in THF, the uncorrected polystyrene equivalents provide a good estimate (within 10%) of absolute MW values for PHA_{mcl}, irrespective of side-chain length.⁴¹

Properties of Thermally Reduced Graphene. X-ray diffraction was used to confirm the oxidation of graphite to GO

and the exfoliation of GO to nonstacked graphene sheets. Details are presented in the Supporting Information.

Transmission electron microscopy (TEM) was used to observe the morphology of graphene sheets precipitated from a DMF suspension, Figure 1. The TEM image indicates that graphene is composed of thin and large wrinkled sheets. Translucent graphene sheets are clearly visible with edges appearing as dark fields.

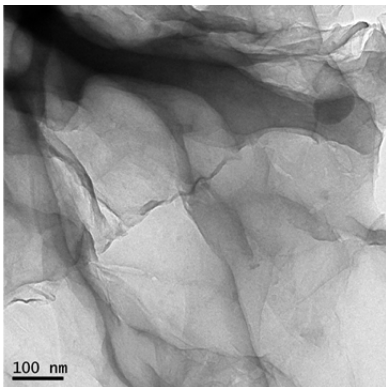


Figure 1. TEM image showing the morphology of TRG sheets.

Properties of PHA–Graphene Nanocomposites. Thermal Stability. The nonoxidative thermal degradation of pure PHA_{mcl} polymers and their graphene nanocomposites was measured between 50 and 350 °C. Measurements were made under nitrogen flow using simultaneous thermal gravimetric analysis (TGA) and differential scanning calorimetry (DSC). Figure 2 shows the effect of graphene loading on different thermal properties. $T_{50\%}$ is the temperature at which 50% of the composite mass remains (Figure 2a). $E_{50\%}$ is the total endothermic heat-load incurred during heating from 270 °C to $T_{50\%}$, and C_p is the specific heat capacity of the composite measured at 270 °C (Figure 2c). For easy comparison with C_p values ($\text{J/g}/^\circ\text{C}$) $E_{50\%}$ values (J/g) have been scaled by the corresponding increase in temperature between 270 °C and $T_{50\%}$ and are presented in units of ($\text{J/g}/^\circ\text{C}$) (Figure 2c). Full thermograms are provided in the Supporting Information. In general, the addition of graphene increases the $T_{50\%}$ values of composites samples: at 2.5% loading $T_{50\%}$ increases by 4–6 °C. One exception to this trend is the PHD–0.5% composite, which shows a decrease in $T_{50\%}$ by -4.6 °C. While increases in $T_{50\%}$ indicate that the addition of graphene can improve the thermal stability of composites, $E_{50\%}$ values provide an alternative perspective. For PHD–1.0% and PHO–2.5% $E_{50\%}$ values increase by 23% and 60% respectively. This indicates improved thermal stability, because more heat is required for degradation to proceed. On the other hand, for PHOe–2.5% and PHD–2.5% $E_{50\%}$ values decrease by 16% and 30% respectively.

Some insight into this result can be gained by considering the specific heat capacity of the samples at 270 °C, just prior to the onset of thermal degradation. The C_p values show an obvious correlation with $E_{50\%}$ values. For PHO the addition of graphene causes a linear increase in the heat capacity of the composite samples. This could be due to an increase in the entanglement density of the composites thereby raising their capacity to store potential energy. Another storage mechanism for potential energy is the formation of hydrogen bonds between the ester groups of polymer chains and hydroxyl and carboxyl moieties

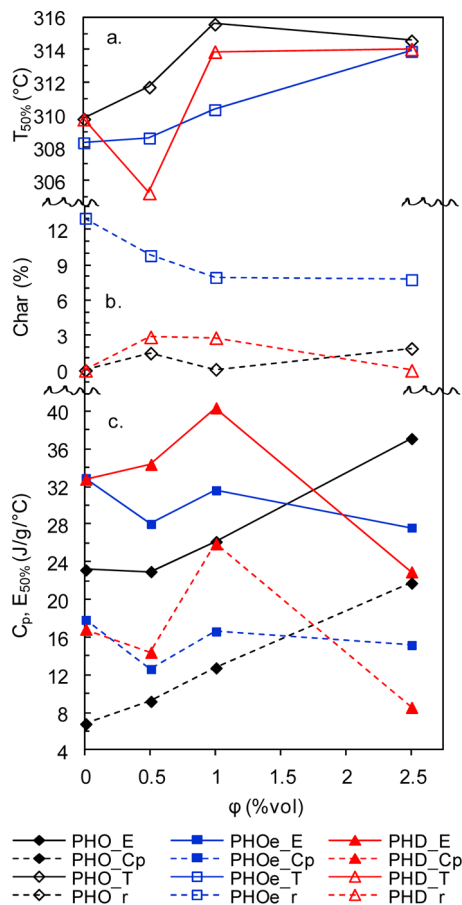


Figure 2. Thermal decomposition data for PHA–graphene composites. (a) Temperature at which 50% of the composite mass has been lost ($T_{50\%}$). (b) Residual char (Char) at 345 °C minus wt % of corresponding graphene loading. (c) Specific heat capacity at 270 °C (C_p) and total endotherm ($E_{50\%}$) when 50% of the composite mass has been lost. $E_{50\%}$ values (J/g) are scaled by the corresponding temperature increase between 270 °C and $T_{50\%}$ to give units equivalent to specific heat capacity ($(\text{J/g})/^\circ\text{C}$).

on the TRG surface. As for why C_p of pure PHO is lower than that of pure PHOe and PHD, it has been shown that C_p is inversely proportional to polymer molecular weight,⁴² and the M_w of PHO is $\sim 25\%$ greater than that of PHOe and PHD. For PHOe, the addition of graphene causes a small decrease in the heat capacity of the composites. We hypothesize that the intercalation of graphene particles within the gel network of PHOe may increase the internal strain of the matrix, thereby consuming some of its capacity to store potential energy. While the PHD–1% composite shows a large increase in heat capacity, the opposite is true for the PHD–2.5% composite. This suggests that under some conditions entanglements with graphene may form less easily for PHD than for PHO, and instead graphene may produce a solvating effect, which reduces the entanglement density of PHD.

The strong correlation between heat capacity and the total endothermic heat-flow indicates that changes to the entanglement density of the composite are a significant factor in controlling the thermal stability of the composites. However, the presence of graphene can provide protection against thermal decomposition by other mechanisms as well. Given that graphene composites show a significant reduction in gas permeability,²⁰ it is likely that their presence retards

degradation by slowing the migration of volatile decomposition gases to the sample surface. Furthermore, it has been shown that the formation of a surface char layer on carbon nanocomposites can act as an additional barrier to gas evolution and may act as a protective heat shield, delaying the rise of sample temperature.⁴³ Ultimately, an increase in the heat capacity of the composite requires an increase in the average kinetic energy of the material, i.e., temperature, to disrupt the physical entanglements that prevent bond breakage necessary to initiate decomposition reactions. Additionally, temperature must increase for gas particles to overcome the graphene barriers that hinder their migration to the surface. For PHO and PHD, the effect of graphene on $T_{50\%}$ appear to saturate by 1% loading, and $T_{50\%}$ values for all three matrices converge to within 0.7 °C by 2.5% loading. This suggests that beyond 1% loading, the kinetics of the decomposition process are governed primarily by the barrier properties of graphene despite the varied entanglement structure of the composites.

For PHD–0.5%, which is the only composite with a reduced $T_{50\%}$, we note that it is also the only composite with an increased $E_{50\%}$ while having a lowered C_p . Thus, the degradation reaction that initiates early in the decomposition of PHD–0.5% is distinctly more endothermic, suggesting that an alternate decomposition process may be at play. Furthermore, we note that among all three polymer matrices the 0.5% composites show higher mass loss rates, $d(\text{mass})/dt$ (mass %/min) than the pure polymer matrices. Data are provided in the Supporting Information. Thus, it is a possibility that the oxygen-containing species on the TRG surface may cause an increase in the decomposition rate, especially if the filler loading is too sparse to hinder escaping gases. For PHOe–0.5%, which experiences an even greater drop in heat capacity but a slight increase in $T_{50\%}$, it is possible that the restriction of polymer motion due to the gel network may provide additional hindrance to gas diffusion, thereby raising the decomposition temperature.

Values for char formation are presented in Figure 2b. Given that single layer graphene has been shown to be stable up to 2600 K,⁴⁴ it is expected to be present as part of the residual char of the degraded composites. Thus, we have adjusted the final char values by subtracting the mass of graphene added to each composite. Note: 0.5, 1.0, and 2.5 vol % graphene ≈ 1.0, 2.5, and 5 wt %. For pure PHO and PHD no residual char is observed; however, for pure PHOe ~13% char was observed. This difference is attributed to the presence of double bonds in the PHOe structure, which can act as a source of free radicals for the initiation of cyclization reactions that lead to the formation of char instead of more volatile compounds.⁴⁵

For PHOe, the addition of graphene results in an unusual reduction in char formation. One possibility may be that oxygen-containing radicals liberated from TRG compete for the alkene groups of PHOe thereby reducing the rate of cyclization reactions. For PHO and PHD, it is interesting that some composites produce char while others do not. Since char formation does not occur between polymer segments alone, it is most likely that additional carbon atoms are retained by bonding to the TRG surface. Presumably, such reactions are aided by the epoxide, alcohol, and carboxyl moieties on the TRG surface. At low graphene loadings polymer chains are the primary reactant at the graphene surface, but at higher loadings, especially in the case of poorly dispersed filler and weak polymer–filler attraction, oxygen-containing species on adja-

cent TRG sheets may compete with polymer chains for reaction, thereby reducing char formation.

Thermal Transitions. The physical transitions of pure and composite samples were measured using DSC. Values for the glass transition temperature (T_g), melting temperature (T_m), specific enthalpy of melting (ΔH_m), specific entropy of melting (ΔS_m), and relative crystallinity (x_c/x_p) are shown in Table 2. Among pure polymer samples, T_m of PHO is higher than that of both PHOe and PHD, which is consistent with previously reported results.^{8,40} We attribute this to the reduction in the crystal-forming ability of the PHOe and PHD polymers caused by disruption of the regularity of the PHO chain by 3HO_{8:1} (3-(R)-hydroxyoctenoate) and 3HD (3-(R)-hydroxydecanoate) monomers, similar to the finding of Noda et al.⁴⁶ Nonetheless, the higher T_m of PHO could also be attributed to its higher molecular weight.²² The effect of graphene on the thermal transitions is demonstrated by a small increase in the T_m of PHO and PHD by ~0.5–3 °C depending on graphene loading.

These results are consistent with a similar increase in T_m with graphene loading reported for other polyoxoester-graphene composites.^{47,48} The increases in T_m for PHO and PHD imply improved perfection in the crystalline lattice; however, this is contradictory to the decreases in ΔH_m which indicate a reduction in crystallinity. Reconciliation of this inconsistency requires consideration of the entropic effects of nanoparticle addition. Recall from thermodynamics, $T_m = \Delta H_m / \Delta S_m$. Thus, for T_m to increase the addition of graphene must cause an even greater decrease in the entropy of the phase transition. We speculate that this is due to an ordering effect of the graphene particles whereby they hinder the rotation and translation of polymer chains within confined spaces. As a necessity, the reduction in entropy must be greater in the melt phase than in solid phase.

For the case of PHOe, the decreases in ΔH_m is smaller (11%, max) compared to PHO and PHD (>42%, max). Part of the reason for this is that PHOe contains fewer crystals that can undergo melting, due to molecular cross-links, which obstruct crystal formation. Contrary to PHO and PHD composites, PHOe composites showed a decrease in T_m by as much as 7.5 °C at only 0.5 vol % graphene loading. Thus, for PHOe the decrease in ΔS_m must be smaller than the decrease in ΔH_m . To explain this alternate effect we hypothesize that graphene particles may be able to intercalate within the gel network of PHOe, thereby creating an isotropic strain within the polymer matrix and raising the enthalpy of the solid state. In the melt phase, however, the added enthalpy of particle intercalation would be less due to random motions in the gel network caused by thermal fluctuations. Essentially, the intercalated particles fall out when polymer movements becomes too large. In addition, ΔS_m would be smaller in the presence of the gel network, which serves to maintain order among the polymer chains during the transition from solid to liquid.

The T_g for pure PHD is significantly lower than that of PHO and PHOe, in agreement with an earlier report.⁸ At 0.5% graphene loading the PHO polymer displays a significant increase in T_g by 3.8 °C while PHD and PHOe show an insignificant decrease by less than 1 °C. As the second order T_g transition is known to be a kinetically controlled effect, this result suggests that the presence of graphene nanoparticles slow the motion of PHO chains by blocking reptation paths and creating entanglements. Further additions of graphene to PHO produce a minimal recovery of the T_g toward its pure polymer value. For the PHD polymer, the addition of graphene causes a

TRG loading ϕ (vol %)	glass transition temp., T_g (°C)				melting temp., T_m (°C)				enthalpy of melting, ΔH_m (J/g)				entropy of melting, ΔS_m (J/kg·K)				relative crystallinity, x_c/x_p
	PHO	PHOe	PHD	PHOe	PHO	PHD	PHOe	PHD	PHO	PHOe	PHD	PHO	PHOe	PHD	PHO	PHOe	
0	-41.9	-39.3	-48.1	53.7	50.7	45.2	15.5	20.9	22.5	47.4	64.5	70.8	1	1	1	1	1
0.5	-38.1	-39.8	-48.7	55.7	43.1	44.9	13.9	18.7	15.3	42.3	59.1	48.2	0.90	0.89	0.89	0.68	0.68
1.0	-38.6	-39.9	-48.8	55.5	46.8	48.1	9.0	20.6	11.1	27.4	64.4	34.5	0.58	0.99	0.99	0.49	0.49
2.5	-39	-38.6	-50.7	54.1	47.2	47.3	12.2	19.9	10.1	37.3	62.1	31.4	0.79	0.95	0.95	0.45	0.45
max change		+3.8°	+0.5°	-2.6°	+2.0°	-7.6°	+2.9°	-42%	-11%	-55%	-42%	-8%	-51%	-42%	-11%	-11%	-55%

sustained decrease in the glass transition temperature with a maximum change of -2.6 °C at 2.5% loading. This result suggests that in PHD, graphene particles provide a plasticization effect by increasing the free volume within the polymer matrix. We attribute this effect to a weaker interfacial attraction between the TRG surface and PHD than with PHO. Moreover, in studies utilizing molecular dynamics simulations, researchers observed that the presence of unattractive nanoparticles in a polymer solution resulted in accelerated molecular motion near the particle surface³¹ and disentanglement of polymer chains with increasing nanoparticle loading.⁴⁹ Because of shielding of the polyester backbone by longer aliphatic appendages we expect the PHD polymer to have a lower molecular affinity for the TRG surface than the PHO polymer; thus, the movement of PHD chains should be less affected by TRG particles. For PHOe, the change in T_g with loading is less significant, ~ 1 °C. This again supports our hypothesis that the presence of cross-linking in PHOe prevents the formation of additional entanglements with the graphene. Other experimental studies combining graphene based fillers with related polyoxoesters have reported both increases⁴⁷ and decreases⁴⁸ in T_g .

Without reference data for the specific enthalpy of melting of pure PHA crystals (ΔH_m^0), the absolute crystallinity of a sample ($x = \Delta H_m/\Delta H_m^0$) cannot be determined from DSC endotherms. However, the specific enthalpy of melting (ΔH_m) data may still be used to infer changes in the relative crystallinity of the composite compared to the crystallinity of the pure polymer. If x_c is the fraction of crystals in the composite and x_p is the fraction of crystals in the pure polymer, then the relative crystallinity of a composite sample (x_c/x_p) may be estimated as $(x_c/x_p) = (\Delta H_m^0/\Delta H_m^0)/(\Delta H_m^p/\Delta H_m^0) = \Delta H_m^c/\Delta H_m^p$. Thus, the addition of graphene to PHO and PHD causes a decrease in the relative crystallinity of the composites to 0.79 and 0.45, respectively, at 2.5% graphene. For PHOe the reduction in crystallinity is minimal, 0.95. The significant increases in the amorphous fraction of PHO and PHD shows that the presence of graphene-polymer entanglements creates a significant hindrance to chain movement and crystal formation. For PHOe the minimal change in crystallinity compared to PHO suggests that the pure PHOe matrix is already more amorphous, thereby giving support to the hypothesis of a supramolecular network in PHOe. Moreover, the presence of covalently bonded polymer–polymer entanglements in PHOe likely precludes the formation of polymer-graphene entanglements.

Similar reductions in the enthalpy of melting and/or crystallization have been observed for various PHA composite systems including: PHB with exfoliated graphite nano-platelets,⁵⁰ PHB-*co*-PHV (13% PHV) with microwave expanded graphite,⁵¹ PHB with organo-modified montmorillonite clay (organo-MMT),⁵² and PHB-*co*-PHV (4% PHV) with organo-MMT.⁵²

Rheological Properties. In order to determine the elastic (G') and viscous (G'') moduli of the composite materials in the melt phase, samples were investigated using oscillatory shear rheometry at 70 °C. Frequency sweep profiles for the pure and composite samples are presented in Figure 3. Data for the pure polymer samples indicates that PHOe has the highest G' followed by PHO then PHD. We suspect that the higher modulus of PHO compared to that of PHD may be due to a greater entanglement density of polymer chains, i.e., lower molecular weight between entanglements (M_e), in the PHO

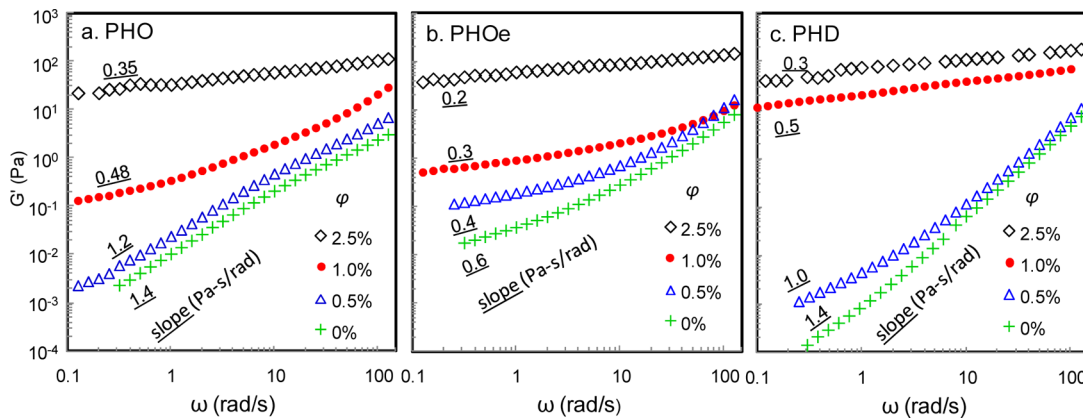


Figure 3. Frequency sweep profiles of PHA–graphene nanocomposites: (a) PHO; (b) PHOe; (c) PHD, ϕ (graphene loading, vol %), G' (elastic storage modulus, Pa), ω (frequency of oscillation, rad/s) The number beside each curve is the calculated slope, Pa-s/rad, at low frequency.

matrix. M_e is known to vary with the cube of the chain packing length (p), and p has a quadratic dependence on the cross-sectional diameter of the polymer chain.²² Because 3HD monomers in PHD increase the cross-sectional area of the polymer chain, the packing length of the PHD chain is expected to be greater. As a result, M_e for PHD is expected to be greater, and its propensity to form entanglements is expected to be reduced.²² Thus, PHO chains with their smaller cross-section are expected to form more entanglements, leading to a greater modulus than less entangled PHD chains.

For PHOe, the presence of double bonds stemming from its aliphatic appendages permits the formation of chemical cross-links between adjacent chains, thereby leading to a greater elastic modulus than the PHO and PHD polymers. In a previous report, researchers produced similar poly(hydroxyalkanoate) polymers synthesized from octane and octene and subjected them to varying intensities of electron-beam radiation to promote cross-linking.⁴⁰ Samples presumed to have a higher degree of cross-linking showed increased modulus values. Thus, in the melt phase, where crystallinity does not contribute to the modulus, the network connectivity provided by cross-linking in the PHOe polymer is responsible for the higher G' for PHOe and the onset of a rubbery plateau at low frequencies, compared to PHO and PHD which have lower values of modulus and display behavior characteristic of the terminal regime.

According to a report by Kazatchkov et al.⁵³ values observed for the crossover frequency, (ω_c), where the storage modulus (G') is equal to the viscous modulus (G''), show an inverse power-law dependence upon M_w , specifically $\omega_c = (M_w)^{-3.7}$ for LLDPE. In our case, ω_c was found to be ~ 70 rad/s for PHO and ~ 40 rad/s for PHOe. Data for G'' not shown. Both matrices had a similar value for the crossover modulus of ~ 1.5 Pa. This difference in ω_c values suggests that the M_w of PHOe is greater than that of PHO. But GPC results show that the M_w of PHO is 71K Da while that of PHOe is 54K Da. We interpret this as another indication of cross-linking in the PHOe matrix, thereby increasing the apparent M_w of linked polymer chains.

In Figure 3a, data for the PHO–graphene composites is presented. As graphene loading increases, G' increases and the slope of the G' versus ω curve begins to decrease in the low frequency region. For purely elastic materials, G' is invariant with respect to changes in the frequency of the applied strain; i.e., the slope of G' versus ω goes to zero. Thus, the reduction in slope of G' versus ω at high graphene loadings indicates the

emergence of elastic behavior due to the presence of a solid-like network structure within the composite. Similar results are obtained for PHOe and PHD, Figures 3b,c. While there is a significant difference in G' of the pure polymers, all three polymers begin to show a definite elastic response by 1% loading, and the differences in G' are almost indistinguishable by 2.5% loading. This suggests that a network of particle–particle interactions dominates the rheology at high loadings while polymer–particle entanglements confer elasticity at lower loadings.

Data for G' versus filler loading (ϕ) may also be used to predict the critical filler loading (ϕ_c) at which percolation of a pseudosolid network first occurs. By fitting a hybrid, power-law model^{54,55} of the form $G' = G'_g ((\phi - \phi_c)/(1 - \phi_c))^\nu$, where G'_g is measured shear modulus of few-sheet graphene,⁵⁶ we calculated the graphene loadings at which network percolation first occurs. See Table 3. Details of the calculations are

Table 3. Model Parameters for Power-Law Fit to Storage Modulus (G') and Electrical Conductivity (σ) Data

		PHO	PHOe	PHD
G'^a	ϕ_c (vol %)	-0.1	-0.8	0.33
	ν	6.0	6.3	5.0
	r^2 ^c	0.999	0.999	0.979
σ^b	ϕ_c (vol %)	0.48	0.40	0.44
	ν	4.3	5.0	5.0
	r^2 ^c	0.999	0.991	0.995

^a G' vs ϕ data fitted with the model $G' = G'_g ((\phi - \phi_c)/(1 - \phi_c))^\nu$. ^b σ vs ϕ data fitted with the model $\sigma = \sigma_g ((\phi - \phi_c)/(1 - \phi_c))^\nu$. ^c r^2 values from linear regression analysis.

presented in the Supporting Information. The negative signs for PHO and PHOe percolation limits arise from error on estimates of ϕ_c very near zero. Moreover, despite the negative signs, the numeric ordering of the values remains meaningful for predicting the relative sensitivity of each matrix to graphene inclusions. Practically, values for the percolation threshold ≤ 0 imply that increases in modulus are realized immediately, upon the smallest addition of filler. This makes sense given that virgin polymer matrices already form a network of entangled polymer chains, whereby stress created by the inclusion of one graphene particle may be transmitted to an adjacent particle, even if the two particles are not in direct contact. Because PHOe already contains a sample-spanning network of covalent cross-links, it is

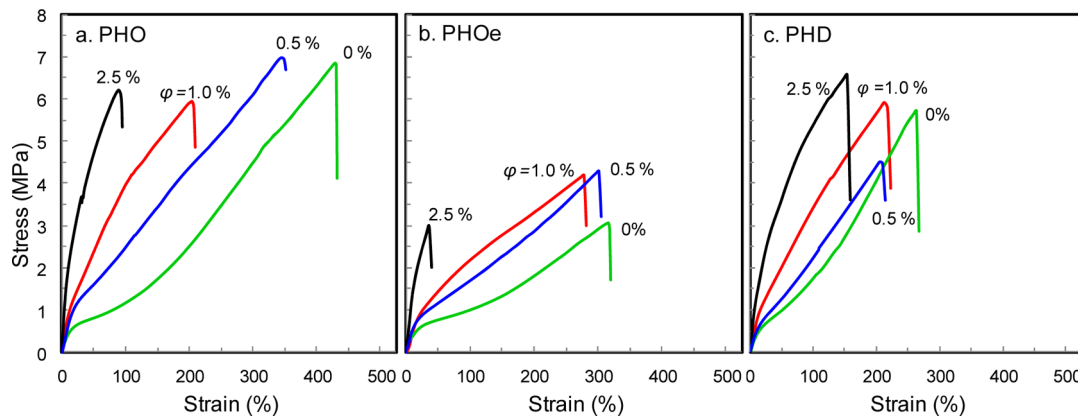


Figure 4. Stress–strain curves for PHA–graphene nanocomposites: (a) PHO; (b) PHOe; (c) PHD ϕ (graphene loading, vol %).

Table 4. Mechanical Properties of PHA–Graphene Nanocomposites

TRG loading ϕ (vol %)	Young's modulus, E (MPa)			ultimate strength, σ (MPa)			elongation at break, ε (%)		
	PHO	PHOe	PHD	PHO	PHOe	PHD	PHO	PHOe	PHD
0	4.5	6.3	5.3	6.4	4.2	5.7	425	316	263
0.5	7.2	6.9	5.7	7	4.3	4.5	346	302	209
1.0	10.9	8.5	11.8	5.6	3.9	5.9	204	293	212
2.5	31	18.8	20.1	6.7	3	6.6	105	34	155
max change	590%	200%	280%	9%	2%	16%	-75%	-89%	-41%

the most sensitive to graphene inclusions and has a φ_c lower than PHO. Alternatively, PHD, which is less likely to participate in molecular entanglements due to its greater packing length and reduced chain length, has a φ_c higher than PHO.

Mechanical Properties. One of the most important benefits of graphene addition is its ability to enhance the mechanical properties of polymer matrices. At low graphene loadings below the percolation threshold, this enhancement is caused by the ability of the graphene particles to promote a greater level of polymer entanglement. At higher graphene loadings beyond the percolation threshold, a continuous graphene network begins to emerge which is capable of direct reinforcement of the polymer matrix. Both effects increase as the attractive molecular forces between the graphene particles and the polymer chains become stronger. Figure 4 shows stress–strain curves for the different composites, while tabular values for Young's modulus (E), ultimate strength (σ), and elongation at break (ε) are presented in Table 4.

The stress–strain profile of pure PHO, PHOe, and PHD is typical of elastomeric polymers and is characterized by three distinct regions: an initial high-modulus region ($\varepsilon < \sim 10\%$), plastic deformation region ($\sim 10\% < \varepsilon < \sim 50\%$), and a strain hardening region ($\sim 50\% < \varepsilon < \sim 200\text{--}300\%$) before fracture at ($\varepsilon > \sim 300\text{--}450\%$.) The increased strain at break observed for the pure PHO polymer, 450%, versus 325% for PHOe, and 275% PHD is likely due to the higher molecular weight of the PHO polymer, i.e. polymer chains must reptate further to break their initial entanglements.

For composite samples, the addition of graphene leads to a significant increase in the Young's modulus. Normalization of modulus values as E_c/E_m , where E_c is the modulus of the composite and E_m is the modulus of the pure matrix, allows equal comparison among the different matrices. Figure 9a shows a plot of the normalized moduli for increasing graphene

loadings. Modulus enhancement is greatest for PHO, 1.6–6.8, lower for PHD, 1.1–3.8, and lowest for PHOe 1.1–3.0. We discuss the disparity among the different matrices in a later section. On the other hand, changes in ultimate strength are less significant, and have minimal correlation with graphene loading. In contrast to modulus values, which increase with graphene loading, values for the elongation at break decrease by a maximum of 41–89% at the 2.5% loading. At this maximum loading, the PHD polymer permits the greatest strain before break, 155%, versus 105% for PHO and 34% for PHOe. We speculate that this may be due to the reduced packing length of the PHD polymer, which allows it to disentangle more easily before reaching its ultimate strength. Regardless of the decrease in elastic range, all composite samples experience a reasonable elongation before break such that they do not become brittle.

Interestingly, we note that as strain increases beyond the plastic deformation region, all composite samples extend with a modulus similar to that of their corresponding pure polymer. This implies that reptating chains eventually escape from their graphene-associated confinements by either disengaging their initial graphene entanglements or by a strain-induced alignment of graphene sheets whereby sliding chains are less likely to encounter new graphene obstacles.

While graphene greatly enhances the modulus of the PHA polymers by 200–590% at 2.5% loading, the effect is even more significant if the decrease in crystallinity is considered. Given that the modulus of a polymer crystal is typically several orders of magnitude greater than the modulus of the amorphous material, the presence of small crystals can alter the mechanical properties of a material similar to the effect of nanoparticle fillers. For example, studies have reported a positive correlation between increases in crystallinity and increases in modulus.^{57,58} Furthermore, the same micromechanical theory used for composite materials has been used to model the behavior of semicrystalline polymers.^{59,60} At 2.5% loading, the relative

crystallinity of PHO, PHOe, and PHD composites compared to the pure polymers is reduced to 0.79, 0.95, and 0.45, respectively; thus, by this effect we would expect the composites to have a lower modulus than the pure polymers.

To account for the effects of reduced crystallinity, we can make an alternate estimate of the modulus enhancement factor as $(E_c/E_m)/(x_c/x_p)$. A derivation of the approximation is given in the Supporting Information. Figure 9a contains a plot of the normalized moduli versus graphene loading, with and without the correction for crystallinity. While there is a significant difference between PHO and PHD for the uncorrected modulus enhancement, the results are almost identical when crystallinity is considered. This alternative estimate suggests that the dispersion and molecular interactions of PHO and PHD with TRG are more similar than originally thought. For PHOe, the effect of crystallinity on modulus enhancement is negligible.

Electrical Conductivity. Another important advantage of polymer-graphene composites is their potential for electrical conductivity. This conduction is possible via the overlap of sp^2 orbitals above the plane of the graphene monolayer. Figure 5

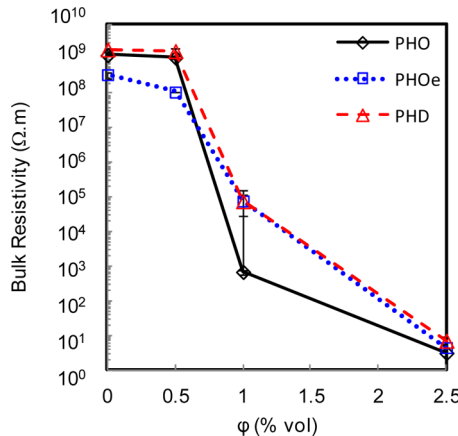


Figure 5. Bulk resistivity (ρ) of PHA-graphene nanocomposites. ϕ (graphene loading, % vol).

shows the bulk resistivity (ρ) of PHA-graphene composites for various graphene loadings. Just before a graphene loading of 0.5%, the formation of a few, continuous, graphene pathways begins to produce a small drop in the resistivity of the composite. By $\phi = 2.5\%$, the bulk resistivity in all three PHA matrices is decreased by >7 orders of magnitude.

To make a more accurate estimate of the electrical conductivity percolation threshold (ϕ_c), we employ a power-law model⁵⁵ of the form $\sigma = \sigma_g ((\phi - \phi_c)/(1 - \phi_c))^\nu$, where σ_g is the conductivity of few-layer graphene, and ν is the “universal constant” for which classical models specify a theoretical value of 2 for geometric percolation. Fitting this model to σ versus ϕ , we calculated the graphene loading at which percolation of an electrically conducting network first occurs. See Table 3. The ϕ_c values for electrical conductivity are distinctly greater than those predicted for rheological percolation and are much more similar among the different polymer matrices. Details of the calculations are presented in the Supporting Information. In rheological and mechanical testing of nanocomposites, improvements in modulus may actually arise before formation of a continuous filler phase due to the aid of polymer entanglements that link distant particles.⁶¹

For this reason, measurements of electrical conductivity are better indicators of geometric network percolation. However, the ϕ_c values predicted from conductivity data may still be below the threshold for true geometric percolation, as the corresponding estimates of ν are all greater than the classical value of 2. Such high ν values have been attributed to quantum tunneling effects, which can permit conductivity between proximal, but nontouching particles.⁵⁵ By analogy, the similarly high values of ν obtained from the rheology percolation models support the hypothesis that polymer entanglements between particles confer network structure well before geometric percolation. Moreover, the wide range of ϕ_c values for rheological percolation, -0.8 to $+0.33$ vol %, indicates significant variation in the molecular interactions of the TRG particles with the different PHA matrices.

Evaluation of Composite Structure. Nanocomposite structure may be described with respect to properties of the nanoparticles, e.g., size, aspect ratio, and dispersion, as well as properties of the polymer entanglements within the matrix, e.g., size and density of entanglements. Direct methods of evaluation include spectroscopy and microscopy while indirect methods use rheological, mechanical, or electrical conductivity measurements to infer structure.

Estimation of A_f and Particle Dispersion from Electrical Conductivity. According to percolation theory for electrically conducting networks, fillers with elongated or expanded geometry such as fibers or sheets possess a lower ϕ_c because they can more readily form a continuous network in a polymer matrix.^{62,63} Moreover, percolation arises most quickly when the particles are distributed in completely random orientations. Thus, ϕ_c for a composite system conveys information about the aspect ratio of the particles as well as their orientation.

For a nanoparticle, the aspect ratio (A_f) is defined as the average diameter of the particle (d) divided by its thickness (t). Crumpling or breaking of graphene particles during exfoliation causes a direct reduction in A_f while particle aggregation, poor dispersion, and strain induced particle alignment during secondary processing can indirectly cause a reduction in the effective A_f .

Assuming a completely random orientation of the nanoparticles, several mathematical models have been proposed to relate ϕ_c to A_f . A semiempirical estimation by Ren et al.⁶² predicts the percolation loading as $\phi_c = (3 \phi_c^s / 2A_f)$, where ϕ_c^s is the percolation volume fraction of spherical particles ($\phi_c^s = 0.3$). A more rigorous model by Celzard et al.⁶³ predicts percolation loading to be bounded between $\phi_c = 1 - \exp((-3.6/\pi A_f))$ and $\phi_c = 1 - \exp((-5.6/\pi A_f))$ for an infinitesimally thin spheroid and a perfect sphere, respectively. On the other hand, a model used by Lu and Mai⁶⁴ predicts $\phi_c = (2.154/A_f)$. Using the values for ϕ_c obtained from conductivity data, values of A_f calculated from the different models are provided in Table 5. The average aspect ratios of all three models is $A_f^{PHO} = 288$, $A_f^{PHOe} = 345$, $A_f^{PHD} = 314$. The similarity in these values indicates that at low graphene loadings there is little difference in the geometry or dispersion of graphene in the three different matrices.

Transmission Electron Microscopy. TEM images are used to visually assess nanofiller dispersion within the matrix. Figure 6 shows TEM images of the composite samples at a loading of 0.5%. The best dispersion of graphene is seen in the PHO sample as indicated by the existence of transparent, likely single layer, graphene sheets. The poorest dispersion is seen in the PHOe sample where the appearance of darkly contrasted and

Table 5. Prediction of Particle Aspect Ratio (A_f) Determined from the Percolation Threshold for Electrical Conductivity (ϕ_c)

ϕ_c (vol %)	A_f^a				
	Ren	Celzard ^b	Lu	av	
PHO	0.48	94	238–370	449	288
PHOe	0.40	113	286–445	539	345
PHD	0.44	102	260–404	490	314

^aRefer to the text for an explanation of the different models. ^bLower and upper bounds correspond to oblate and spherical limits.

parallel edges is indicative of multilayer graphene aggregates. Similar dark edges are also seen in the PHD sample, but the more diffuse coloration suggests better separation and more randomly oriented graphene layers than in the PHOe sample. As presented in the previous discussion on electrical conductivity, percolation of a continuous graphene phase was estimated to occur at between 0.4 and 0.5% for all three matrices.

Scanning Electron Microscopy. Additionally, SEM images of fracture topology can be used to infer information about the entanglement structure of nanocomposites. See Figure 7. Images are taken from the fractured surfaces of test specimens following tensile testing shown in Figure 4. When comparing among pure polymer samples only, i.e., 0% graphene loading, both the PHO and PHD samples show smooth surfaces while the PHOe sample is more textured. This surface roughness suggests inhomogeneity within the PHOe matrix, likely due to the presence of cross-linking within the matrix.

With respect to graphene content, samples with increased filler loading tend to show greater surface roughness. We speculate that deeper cavities on the fracture surface, e.g., Figure 7a, PHO–0.5%, are caused by pull-out of more rigid, graphene-polymer entanglements from the softer, bulk matrix. This result indicates that even at a minimal filler loading of 0.5%, PHO molecules are capable of forming large entanglement masses with the graphene particles. We note that the characteristic size of features on the fracture surface are several micrometers in scale, yet the graphene particles used for reinforcement are on the order of tenths of micrometers in scale. Thus, the polymer entanglements that are induced by the presence of the graphene inclusions persist well beyond the characteristic size of the nanoparticles. The greatest variety of surface topology is seen for the PHO composites, which shows a strong correlation with the significant changes observed in the elongation at break values. See Figure 4a. Interestingly, we find that the PHO–0.5% composite exhibits a greater surface

roughness than the PHO–2.5% composite. Thus, it may be that as the number of graphene particles increases, the large entanglement masses that surround individual particles merge and create a more uniform entanglement density. For PHD composites shown in Figure 7c, only a minimal increase in surface roughness is seen with graphene loading. This is consistent with the observation that the PHD composites all showed similar strain and modulus values just prior to fracture. See Figure 4c. We interpret this to mean that at the point of fracture the presence of graphene nanoparticles had minimal influence on the entanglement structure of the polymer. It may be that a strain induced alignment of the particles and/or disentanglement of polymer chains from the graphene particles resulted in greater homogeneity in the polymer cross section. Likewise, PHOe samples presented in Figure 7b show little change in their fracture topology until the 2.5% graphene loading when the pull-out morphology appears. This again reflects the stress-strain trends seen in Figure 4b. Thus, we infer that only at the 2.5% graphene loading do significant polymer–graphene entanglements form within the PHOe matrix. It is possible that the preexisting cross-links in the PHOe matrix prevented the formation of polymer entanglements with graphene particles until enough particles were present to significantly disrupt the cross-linked network. Ultimately, these images demonstrate that free PHO molecules engage in polymer entanglements more readily than PHD molecules or cross-linked PHOe molecules.

Estimation of A_f and Particle Dispersion from Modulus Enhancement. According to micromechanical theory the enhancement of mechanical properties in composite materials^{30,65,66} is strongly impacted by both A_f as well as particle orientation.^{30,62,63} Particles with large aspect ratios, such as graphene sheets and carbon nanotubes, produce a greater increase in modulus than spherical ones. When a collection of randomly dispersed graphene particles are all oriented in the same direction, modulus enhancement is maximum and points in the direction normal to the graphene surface. Alternatively, when the orientation of particles is completely random, modulus enhancement is reduced, but the property becomes isotropic. Unlike the percolation of electrical conductivity, increases in modulus can occur even when reinforcing particles do not form a continuous network. An alternate technique to estimate the A_f and orientation of nanoparticles within a polymer matrix is by using the micromechanical equations of Tandon and Weng.³⁰ These equations based on earlier work by Mori and Tanaka⁶⁶ describe the enhancement in modulus of a polymer matrix due to the addition of small filler particles in the form of either oblate or prolate spheroids with varying degrees

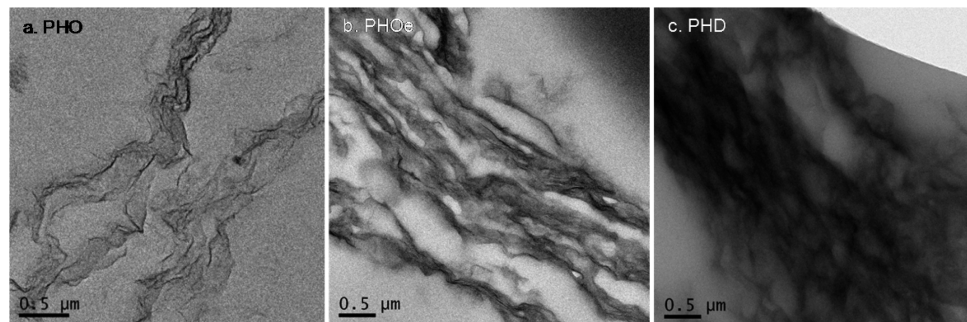


Figure 6. TEM micrographs of PHA–graphene nanocomposites: (a) PHO; (b) PHOe; (c) PHD. For all samples the graphene loading is 0.5 vol %.

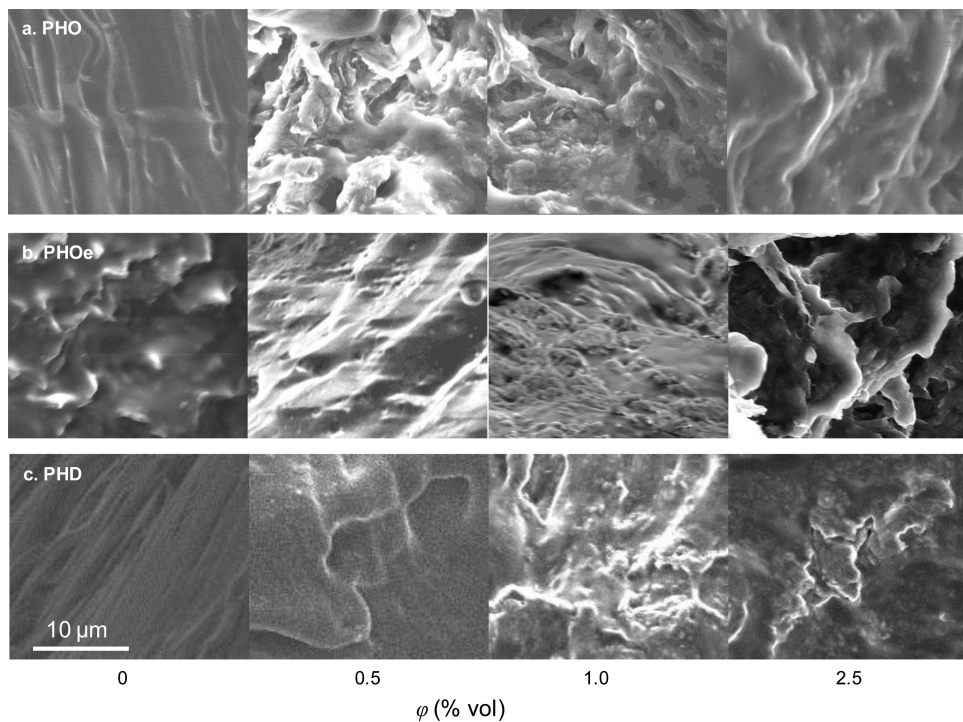


Figure 7. SEM micrograph of PHA–graphene nanocomposites. Panels: (a) PHO; (b) PHOe; (c) PHD.

of A_f . The equations are used in conjunction with experimental data for E_c/E_m versus φ , where E_c is the composite modulus, E_m is the pure polymer modulus, and φ is the volume fraction of filler within the composite. Values for the filler modulus (E_f), and Poisson ratio of the matrix and the filler (ν_m , ν_f) are also required for the calculations. Details of the equations are presented in the Supporting Information. Figure 9a is a plot of E_c/E_m versus φ for the composites in this study. Calculations with the Tandon and Weng equations predict $A_f^{PHO} = 309$, $A_f^{PHOe} = 97$, and $A_f^{PHD} = 151$. The value of A_f^{PHO} predicted by this method is similar to the ones predicted by percolation theory, while the values for A_f^{PHOe} and A_f^{PHD} are significantly smaller. However, when the modulus enhancement values are corrected for crystallinity by $(E_c/E_m)/(x_c/x_p)$, the resulting A_f values are, $A_f^{PHO} = 435$, $A_f^{PHOe} = 106$, and $A_f^{PHD} = 425$. This suggests that the behavior of the PHO and PHD matrices are actually, very similar. For PHOe, the lower value of A_f predicted by modulus enhancement, $A_f = 97$, compared to percolation theory, $A_f = 345$, suggests that the presence of covalent cross-links somehow prevents stress transmission to the graphene particle.

While the explanation of crystallinity seems to account of the difference in modulus between PHO and PHD, we note that the pull-out morphology seen in SEM images of PHO and PHOe fracture surfaces is not seen in PHD. Also, PHO and PHOe experience a 75% and 89% reduction in ε at 2.5% graphene loading, while for PHD the reduction in ε is only 41%. This suggests that under high stresses, PHD relinquishes its graphene entanglements more easily, possibly due to a reduced interfacial attraction.

Effect of Particle–Polymer Interfacial Forces on Modulus Enhancement. Another important point when considering filler effects is the nature of the interfacial forces between the polymer and particle. In simulations it has been shown that attractive forces at the particle surface can result in a greater entanglement density surrounding the particle surface,²⁵

thereby leading to increases in modulus. In choosing to compare the composites according to A_f values, we note that the Tandon and Weng equations, which assume perfect lamination between matrix and filler and a no-slip condition at the interface, do not account for variations in interfacial attraction and the phenomenon of entanglements. Alternatively, Lu et al. have developed a similar set of micro-mechanical equations that do account for the effects of entanglements caused by interfacial forces.⁶⁷ In their results, increasing the volume or modulus of the entanglement “interphase” surrounding each nanoparticle resulted in a linear increase in composite modulus similar to the linear trend seen with particle size. Thus, we assert that A_f values calculated from the basic Tandon and Weng equations are also an indicator of strong interfacial forces as well as particle geometry and the quality of dispersion.

Given the presence of epoxide, hydroxyl, and carbonyl groups on the TRG surface and ester linkages along the poly(hydroxyalkanoate) chain, the possibility does exist for the formation of polarity-based van der Waals attractions as well as hydrogen bonding. However, in PHA_{mcl} polymers the presence of long aliphatic extension from the polyester backbone would likely reduce the intensity of such interactions due to steric-hindrance of oxygen atoms along the polymer backbone. According to this hypothesis, we would expect that the PHO polymer with its shorter aliphatic appendages would be more available for bonding interactions with TRG particles than the PHD polymer. Thus, PHO would exhibit a greater increase in the normalized modulus than PHD. In a related study of TRG composites, Kim et al.⁶⁸ demonstrated that functionalization of polyethylene with different polar moieties capable of hydrogen bonding resulted in greater enhancements of the Young's modulus compared to TRG composites of unmodified polyethylene. Furthermore, samples prepared by solvent blending had greater modulus enhancement than those

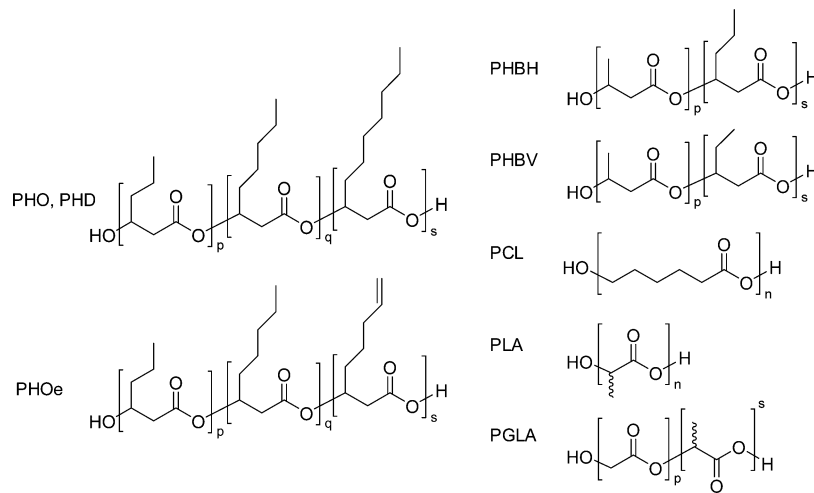


Figure 8. Structures of various biodegradable polyoxoesters. Monomers <1% (wt) of polymer composition are not depicted in the structures.

Table 6. Properties of Biodegradable Polyoxoester-Layered Carbon Nanocomposites

polymer-filler	matrix modulus E_m (MPa)	particle diam ^u d (nm)	aspect ratio ^v A_f (d/t)					sonic time (h)
			measd	calcd	oxygen content C:O ^w	dispr method ^x		
PHO-TRG ^a	4.5	500 ^b	700–1500 ^c	309	10:1 ^d	TCM	0.12	
PHOe-TRG ^a	6.3	500 ^b	700–1500 ^c	97	10:1 ^d	TCM	0.12	
PHD-TRG ^a	5.3	500 ^b	700–1500 ^c	151	10:1 ^d	TCM	0.12	
PHBH-EG ^e	292	13000 ^f	240–570 ^g	325	58:1 ^h	TCM	0.16	
PHBV-MEG ⁱ	85.7	5000 ^j	2500 ^j	11	94:1 ^j	TCM	0.16	
PLA-GNP ^k	1800	5000 ^k	600–900 ^k	1110	22:1 ^l	TCM	2	
PLA-TRG ^m	3000	500 ⁿ	700–1500 ^c	81	10:1 ^d	melt	0	
PLA-GO ^k	1800	500 ^k	300–800 ^o	1405	2:1 ^d	DMK/TCM	5	
PCL-TRG ^p	107	500 ⁿ	700–1500 ^c	846	10:1 ^d	TCM	2	
PCL-GO ^q	340	600 ^r	400–900 ^o	53	2:1 ^d	DMF	24	
PLGA-GO ^s	110	200 ^s	150–300 ^o	191	2:1 ^d	DMF/DCM	24	
PLGA-GO ^t	203	500 ^t	300–800 ^o	155	2:1 ^d	DMF	1	

^aPolymers in this study. ^bReference 33. ^cReferences 33 and 75. ^dReference 76. ^eReference 48. ^fReference 77. ^gReferences 78–80. ^hReference 74. ⁱReference 69. ^jReference 51. ^kReference 81. ^lReference 47. ^mReferences 76, 82, and 83. ⁿReference 33. ^oReferences 76 and 83. ^pReference 70. ^qReference 71. ^rReference 84. ^sReference 73. ^tReference 72. ^uParticle diameter was usually given as a range: here we present an estimated median value. ^vAspect ratio (measd) was estimated by dividing the range of particle diameters by the estimated median value for particle thickness that was found in the specified references. Aspect ratio (calcd) was determined from E_c/E_m versus φ data using the equations of Tandon and Weng. ^wC:O (the ratio of carbon to oxygen atoms in the filler material). ^xSolvents: TCM (chloroform), DCM (dichloromethane) DMK (acetone), DMF (*N,N*-dimethylformamide).

prepared by melt blending, presumably due to better dispersion of the filler.

Modulus Enhancement in Other Biodegradable, Polyester Nanocomposites. To further explore the relationships among polymer structure, particle size, and surface chemistry, we compared our results to other studies combining layered carbon fillers with biodegradable polyesters. All the studies we considered used some form of graphite-derived filler; however, variations in synthesis technique and exfoliation procedure resulted in different particle sizes, aspect ratio, and oxygen content of the nanoparticles. The systems considered include: poly(3-(R)-hydroxybutyrate)-co-poly(3-(R)-hydroxyhexanoate) (PHBH, 13% 3HH) with expanded graphite (EG),⁴⁸ poly(3-(R)-hydroxybutyrate)-co-poly(3-(R)-hydroxyvalerate) (PHBV, 13% 3HV) with microwave expanded graphite (MEG),⁵¹ polylactide (PLA) with graphene nanoplatelets (GNP),⁴⁷ graphite oxide (GO),⁴⁷ or thermally reduced graphene (TRG),⁶⁹ poly(*ε*-caprolactone) with TRG⁷⁰ or GO,⁷¹ and polyglycolide-co-polylactide (PGLA, 50% lactide) with GO.^{72,73} Figure 8 shows the chemical structure of each

polymer, and Table 6 provides the details for each nanocomposite study. For a review of preparation and exfoliation techniques for graphene and graphite oxide see Kim et al.²⁰ and Dreyer et al.³² Figure 9b provides a plot of E_c/E_m versus φ for the other nanocomposites in the literature, which was used to calculate A_f for each. In calculating the slopes of the E_c/E_m versus φ lines, we used only the first three loading fractions from each data set, including 0%, where dispersion is expected to be the best and the slope is a maximum. All the considered polymers have a similar polyoxoester backbone; however, they differ in the linear density of ester bonds and the size of aliphatic appendages stemming from the backbone. Young's moduli of the polymers range on the order of 1 to 1000 MPa and include both glassy and semicrystalline polymers. The equations of Tandon and Wang predict that for a given loading volume of filler, low modulus polymers will experience a proportionally greater enhancement in modulus than will high modulus polymers.²⁰ Thus, the calculation of A_f from the Tandon and Weng equations allows normalization of E_c/E_m

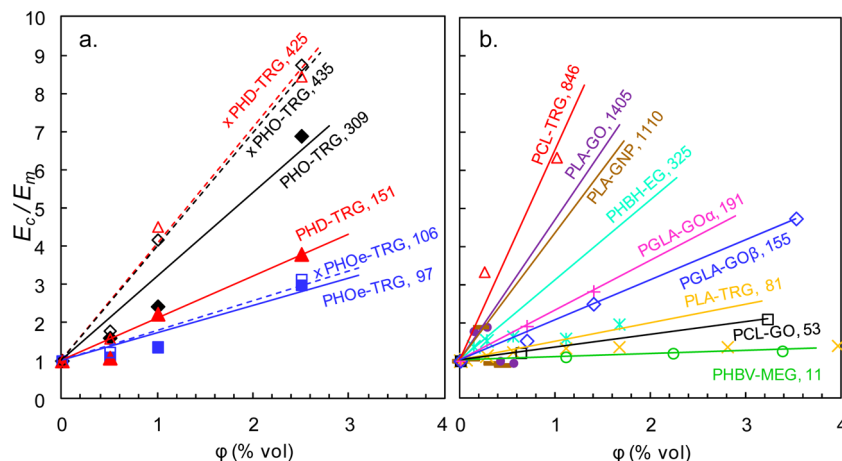


Figure 9. Relative modulus increase and effectiveness of dispersion of layered carbon nanofillers in biopolymer nanocomposites. (a) Nanocomposites in this report: PHO-TRG (\blacklozenge), PHOe-TRG (\blacksquare), PHD-TRG (\blacktriangle), xPHO-TRG (\lozenge), xPHOe-TRG (\square), and xPHD-TRG (\triangle). “x” before the abbreviation denotes data corrected for reduced crystallinity. (b) Nanocomposites in the literature: PLA-GO (\bullet) PLA-GNP (—), PHBH-EG (*), PLA-TRG (\times), PHBV-MEG (\circ), PGLA-GO $^\alpha$ (+), PGLA-GO $^\beta$ (\diamond), PCL-TRG (\triangle), and PCL-GO (\square). E_c and E_m are the modulus for the composite and unfilled matrix, respectively. The number next to each polymer name is the filler’s average aspect ratio (A_f) calculated using the Tandon and Weng model.

versus ϕ data so that an equal comparison of reinforcement effects can be made.

We judge the quality of reinforcement for each system by comparing the value of A_f predicted from the Tandon and Weng equations to the A_f determined from particle measurements. In some cases measured A_f were taken from spectroscopy or microscopy data from the actual composite, and in others A_f values were determined from measurements of pure nanofiller.

Generally, the data show that the use of particles with a larger aspect ratio contributes to greater enhancements in the relative modulus. Polymers with small aliphatic appendages or none, e.g., PLA-GO, PLA-GNP, PHBH-EG, PCL-TRG, and PGLA-GO, tend to give values of A_f near or above the measured A_f , while PHO, PHOe, and PHD, all with longer aliphatic appendages, give values of A_f well below the A_f value measured from pure nanofiller (Table 6). This is consistent with our hypothesis that steric hindrance from long aliphatic appendages may disrupt hydrogen bonding and other non-covalent interactions with oxygen molecules on the TRG surface. However, it is possible that use of a longer sonication period for the TRG used in our study could have resulted in increased value of A_f due to better exfoliation of multilayer particles.⁸⁴ We also note that the highest value of A_f 140S, occurs when PLA is paired with GO. Again this suggests that the additional interfacial attraction due to the presence of extra oxygen moieties on the surface of GO may give rise to strong reinforcement effects.

However, the data set does contain exceptions to these observations. The most conspicuous is the low modulus of PLA-TRG composites given that PLA-GO and PLA-GNP both show a much greater modulus enhancement. For PLA-TRG we attribute the low value of A_f to the melt blending technique used for graphene dispersion.⁶⁸ As a result of this process, the TRG received no sonication prior to mixing which likely resulted in poor exfoliation of graphene particles and a reduced aspect ratio. Furthermore, the viscosity of melt phase PLA is likely much higher than solvated PLA thus requiring greater mixing times for melt compounding.

The modulus enhancement for PHBV is also unexpectedly low given the much greater modulus enhancement for PHBH, which is structurally similar. Here we note that the oxygen content of the microwave expanded graphite used for PHBV (C:O = 94:1) is the lowest among all filler materials. We speculate that reduced intermolecular attraction between the polymer and filler may have led to poor dispersion and minimal reinforcement effects.

Next, we draw attention to the result of the PCL-GO composites. Given the absence of any aliphatic appendages along the PCL backbone and the use of GO for filler, we expect the presence of strong interfacial adhesion in the composite, thus the minimal increase in modulus is an unexpected result. While the solvent used for this study, dimethylformamide (DMF), is a good solvent for graphite oxide,⁸⁵ it is a poor solvent for PCL, especially as M_w increases beyond 65 000:⁸⁶ for the PCL-GO composite, the M_w was 300 000. Thus, poor physical dispersion of the GO in PCL may have contributed to the low modulus enhancement.

For PGLA-GO, we obtained data from two, very similar studies; however, we do observe a small disparity in the degree of reinforcement. In the first study⁷³ which produced the highest calculated value of A_f 191, we note that the researchers used a 24 h sonication period to disperse the GO, and they dissolved the polymer in dichloromethane which is known to be a strong solvent for PGLA. In the second study⁷² which produced a lower calculated value A_f 155, the authors sonicated the GO for only 1 h and dissolved the PGLA in dimethylformamide, a less effective solvent, thus requiring them to heat the polymer to 60 °C.

For several of the polymer systems including: PLA-GO, PLA-GNP, PLA-TRG, and PHBH, the modulus either remains constant or even decrease with increasing graphene loading beyond ~0.3 vol %. This suggests a poor dispersion of graphene possibly induced by aggregation at higher graphene loadings.

CONCLUSIONS

The purpose of this study was to explore how variations in the molecular structure of elastomeric PHA_{mcl} polymers affect their

performance in TRG nanocomposites. Depending on matrix type, the Young's modulus increased by 180–590%, and the elongation at break decreased by 41–89% at the 2.5% loading. However, it is likely that the magnitude of the modulus enhancements would have been higher if it were not for a decrease in matrix crystallinity by 15–55%.

Percolation of an electrically conducting, graphene, network was observed to occur between a volume loading of 0.4–0.5%, and an increase in electrical conductivity by $>10^7$ orders was observed at 2.5% loading. Conversely, rheology data indicated that percolation of a pseudosolid network based on graphene-polymer entanglements occurred at a distinctly lower graphene loading close to 0 vol %.

The addition of graphene to PHA_{mcl} also showed an effect on the thermal stability of the composites: for $T_{50\%}$ changes varied between an increase of 5.8 °C and a decrease of −4.5 °C. For the endothermic heat requirement at $T_{50\%}$, values varied between an increase of 60% and a decrease of −30%. Moreover, $E_{50\%}$ values showed a strong correlation with variation in the heat capacity of composites, likely due to changes in the entanglement structure of polymer chains.

Comparison of modulus improvements among the three different matrices was done by calculating values for A_f from normalized modulus data. Initially, the results indicated that reinforcement in PHO, $A_f^{PHO} = 309$, was more effective than in PHD, $A_f^{PHD} = 151$, but when the effects of crystallinity change were considered, PHO and PHD showed similar improvements in modulus, $A_f^{PHO} = 435$ and $A_f^{PHD} = 425$, respectively. Still, differences in the elongation at break and SEM fracture topology suggest that PHD may disentangle from the graphene particles more easily than PHO. We speculate this may be due to the longer packing length of PHD, i.e. its larger diameter, or a reduction in the interfacial attraction between PHD and TRG due to steric shielding of oxygen atoms along the polyester backbone.

In the covalently cross-linked PHOe matrix, $A_f^{PHOe} = 97$, modulus improvements were significantly lower than in the uncross-linked PHO, $A_f^{PHO} = 309$, even when sample crystallinity was considered. Presumably, the network structure of PHOe precludes the formation of strong entanglements with the graphene particles. This hypothesis is supported by SEM images of fractured surfaces following extension testing. The rough surface topology of the PHO–0.5% graphene composite suggests the formation of dense polymer–graphene entanglements. Only at 2.5% graphene loading does PHOe show a similarly rough, pull-out morphology. An interesting experiment would be to measure the reinforcement effects when matrix cross-linking is performed after graphene dispersion.

Our survey of other composite systems in the literature highlights the numerous factors, which can control the effectiveness of nanoparticle reinforcement. These include: polymer chemistry, particle aspect ratio, chemical modifications on the nanofiller surface, dispersion method (i.e., solvent versus melt), solvent choice for both graphene and polymer, and duration of sonication treatment for exfoliation. Comparison of our results against other, in-class, biopolymers gives support for our hypothesis that strong interfacial interactions can increase the degree of modulus enhancement in PHAs. Longer aliphatic appendages present in PHA_{mcl} polymers may preclude the formation of hydrogen bonds and other noncovalent interactions with the TRG nanoparticles compared to less bulky polymers such as PHB-*co*-PHH, PLA, PCL, and PGLA that showed greater improvements in relative modulus. The use of

GO with its higher fraction of epoxide, hydroxyl, and carbonyl moieties may be a way to further improve interfacial attraction with PHA_{mcl} similar to the way in which GO proved very effective with PLA⁴⁷ and PGLA⁷² systems. Additionally PHA_{mcl} could itself be functionalized to promote hydrogen bonding, e.g., with the use of terminally substituted ω -hydroxy fatty acids⁸⁷ as monomer feedstocks.

Furthermore, good dispersion technique is essential when preparing polymer graphene composites. The saturation of modulus enhancement with graphene loading seen in some composites is likely an indication of poor dispersion. While sonication can be a useful tool for exfoliation, which increases the aspect ratio of particles, it can also break graphene particles and lessen their aspect ratio when the duration of the treatment is extended.⁸⁴ Comparison among different studies in the field would benefit from a quantitative approach to this technique by detailed reporting of the graphene concentration in the dispersant, duration of sonication times, and power density (power/volume) used for exfoliation. Furthermore, care should be taken to choose a solvent, which is effective at solubilizing both the nanoparticle and the polymer. In cases of high viscosity in either polymer melts or solutions, estimation of mixing time can help ensure proper dispersion, i.e., good micromixing at the length scale of the nanoparticles. The estimate of mixing time depends on filler density, solution viscosity, volumetric power density, and geometry of the mixing equipment.

We envision several practical applications for PHA–graphene composite technology. First, the significant improvements in polymer stiffness afforded by graphene reinforcement greatly expand the useful mechanical range of PHA elastomers. Second, the added property of electrical conductivity could allow the proliferation of PHA based materials into previously unrecognized applications. These may include for instance, biodegradable options for packaging of charge sensitive electronic circuit boards and charge dissipating floor coverings for use in static-sensitive manufacturing processes. Because poly(hydroxyalkanoate)s are also biocompatible the possibility may exist for the use of these materials in implantable devices or as tissue scaffolds with electrical conductivity. However, what remains the most significant impediment to greater proliferation of PHA_{mcl} polymers is their low melting point, 45–55 °C, compared to PHB with a melting point of 175 °C. For PHO and PHD graphene addition resulted in a small increase in T_m by up to 3 °C but caused a reduction in T_m by as much as −8 °C for PHOe. Fortunately with the use of blends, copolymers, cross-linking, and more recently PHA block copolymers, it is likely that a PHA_{mcl} material can be created with a melting temperature sufficiently high to meet the requirements of current engineering plastics.

■ ASSOCIATED CONTENT

● Supporting Information

- (1) Method and schematic of poly(hydroxyalkanoate) biosynthesis, (2) method and results of graphene characterization, (3) TGA and DSC thermograms for PHA–graphene decomposition studies, (4) method and results for estimating the percolation threshold from rheology data, (5) method and results for estimating the percolation threshold from electrical conductivity data, (6) equations and parameter values for computing A_f using the micromechanical theory of Tandon and Weng, and (7) derivation of a corrected modulus enhancement

factor to account for changes in crystallinity. This material is available free of charge via the Internet at <http://pubs.acs.org>.

AUTHOR INFORMATION

Corresponding Authors

*(A.A.A.) E-mail: aabdala@pi.ac.ae. Telephone: 971-2-607-5584. Fax: 971-2-6075200.

*(F.S.) E-mail: srienc@umn.edu. Telephone: 612-624-9776. Fax: 612-625-5780.

Author Contributions

The manuscript was written through the contributions of all authors. All authors have given approval to the final version of the manuscript.

Notes

The authors declare no competing financial interest.

[†]Part of this material was originally presented at the 244th ACS National Meeting in Philadelphia, PA (August 19–23, 2012).

ACKNOWLEDGMENTS

The authors would like to acknowledge the following people and organizations for their contribution to the manuscript: Mr. Daniel P. Rouse of the University of Minnesota for synthesis and purification of the poly(hydroxyalkanoate)s polymers, Mr. Hussain Arwani (a Petroleum Institute visiting student from the University of Waterloo) for assistance in preparation and characterization of nanocomposites (while at the Petroleum Institute), Dr. Thomas Krick and the Center for Mass Spectrometry and Proteomics, Dr. Fang Zhou of the Characterization Facility, and Dr. David Giles of the Polymer Characterization Lab. This work was financially supported by the Abu Dhabi Minnesota Institute for Research Excellence (ADMIRE).

REFERENCES

- (1) Reis, M. A. M.; Serafim, L. S.; Lemos, P. C.; Ramos, A. M.; Aguiar, F. R.; Loosdrecht, M. C. M. *Bioprocess Biosystems Eng.* **2003**, *25* (6), 377–385.
- (2) Chen, G.-Q.; Wu, Q. *Biomaterials* **2005**, *26* (33), 6565–6578.
- (3) Wang, F.; Lee, S. Y. *Appl. Environ. Microbiol.* **1997**, *63* (12), 4765–4769.
- (4) Lee, W.-H.; Loo, C.-Y.; Nomura, C. T.; Sudesh, K. *Bioresour. Technol.* **2008**, *99* (15), 6844–6851.
- (5) Castilho, L. R.; Mitchell, D. A.; Freire, D. M. G. *Bioresour. Technol.* **2009**, *100* (23), 5996–6009.
- (6) Ishizaki, A.; Tanaka, K.; Taga, N. *Appl. Microbiol. Biotechnol.* **2001**, *57* (1–2), 6–12.
- (7) Barrett, J. S. F.; Srienc, F. In *Green chemistry for the production of biodegradable, biorenewable, and biocompatible polymers*; John Wiley & Sons, Inc.: New York, 2011; pp 329–359.
- (8) Gross, R. A.; DeMello, C.; Lenz, R. W.; Brandl, H.; Fuller, R. C. *Macromolecules* **1989**, *22* (3), 1106–1115.
- (9) Liu, W.; Chen, G. Q. *Appl. Microbiol. Biotechnol.* **2007**, *76* (5), 1153–9.
- (10) Fernandes, E. G.; Pietrini, M.; Chiellini, E. *Biomacromolecules* **2004**, *5* (4), 1200–1205.
- (11) Botana, A.; Mollo, M.; Eisenberg, P.; Torres Sanchez, R. M. *Appl. Clay Sci.* **2010**, *47* (3–4), 263–270.
- (12) Maiti, P.; Batt, C. A.; Giannelis, E. P. *Biomacromolecules* **2007**, *8* (11), 3393–3400.
- (13) Xu, C.; Qiu, Z. *Polym. Adv. Technol.* **2011**, *22* (5), 538–544.
- (14) Yun, S. I.; Lo, V.; Noorman, J.; Davis, J.; Russell, R. A.; Holden, P. J.; Gadd, G. E. *Polym. Bull.* **2010**, *64* (1), 99–106.
- (15) Li, B.; Zhong, W.-H. *J. Mater. Sci.* **2011**, *46* (17), 5595–5614.
- (16) Byrne, M. T.; Gun'ko, Y. K. *Adv. Mater.* **2010**, *22* (15), 1672–1688.
- (17) Verdejo, R.; Bernal, M. M.; Romasanta, L. J.; Lopez-Manchado, M. A. *J. Mater. Chem.* **2011**, *21* (10), 3301–3310.
- (18) Lee, C.; Wei, X.; Kysar, J. W.; Hone, J. *Science* **2008**, *321* (5887), 385–388.
- (19) Bunch, J. S.; Verbridge, S. S.; Alden, J. S.; van der Zande, M.; Parpia, J. M.; Craighead, H. G.; McEuen, P. L. *Nano Lett.* **2008**, *8* (8), 2458–2462.
- (20) Kim, H.; Abdala, A. A.; Macosko, C. W. *Macromolecules* **2010**, *43* (16), 6515–6530.
- (21) Everaers, R.; Sukumaran, S. K.; Grest, G. S.; Svaneborg, C.; Sivasubramanian, A.; Kremer, K. *Science* **2004**, *303* (5659), 823–6.
- (22) Hiemenz, P. C.; Lodge, T. P. *Polymer Chemistry*, 2nd ed.; CRC Press: Boca Raton, FL, 2007.
- (23) de Gennes, P. G. *J. Chem. Phys.* **1971**, *55* (2), 572–579.
- (24) Sarvestani, A. S. *Eur. Polym. J.* **2008**, *44* (2), 263–269.
- (25) Kabanemi, K. K.; Hétu, J.-F. *J. Non-Newtonian Fluid Mech.* **2010**, *165* (15–16), 866–878.
- (26) Toepperwein, G. N.; Karayannidis, N. C.; Riggleman, R. A.; Kröger, M.; de Pablo, J. J. *Macromolecules* **2011**, *44* (4), 1034–1045.
- (27) Schneider, G. J.; Nusser, K.; Willner, L.; Falus, P.; Richter, D. *Macromolecules* **2011**, *44* (15), 5857–5860.
- (28) Riggleman, R. A.; Toepperwein, G.; Papakonstantopoulos, G. J.; Barrat, J.-L.; de Pablo, J. J. *J. Chem. Phys.* **2009**, *130* (24), 244903–6.
- (29) Knauert, S. T.; Douglas, J. F.; Starr, F. W. *J. Polym. Sci., Part B: Polym. Phys.* **2007**, *45* (14), 1882–1897.
- (30) Tandon, G. P.; Weng, G. *J. Polym. Compos.* **1984**, *5* (4), 327–333.
- (31) Masnada, E.; Merabia, S.; Couty, M.; Barrat, J.-L. *Soft Matter* **2013**, *9* (44), 10532–10544.
- (32) Dreyer, D. R.; Park, S.; Bielawski, C. W.; Ruoff, R. S. *Chem. Soc. Rev.* **2010**, *39* (1), 228–240.
- (33) McAllister, M. J.; Li, J.-L.; Adamson, D. H.; Schniepp, H. C.; Abdala, A. A.; Liu, J.; Herrera-Alonso, M.; Milius, D. L.; Car, R.; Prud'homme, R. K.; Aksay, I. A. *Chem. Mater.* **2007**, *19* (18), 4396–4404.
- (34) Lageveen, R. G.; Huisman, G. W.; Preusting, H.; Ketelaar, P.; Eggink, G.; Witholt, B. *Appl. Environ. Microbiol.* **1988**, *54* (12), 2924–2932.
- (35) Mantzaris, N. V.; Kelley, A. S.; Daoutidis, P.; Srienc, F. *Chem. Eng. Sci.* **2002**, *57* (21), 4643–4663.
- (36) Pederson, E. N.; McChalicher, C. W. J.; Srienc, F. *Biomacromolecules* **2006**, *7* (6), 1904–1911.
- (37) Riis, V.; Mai, W. *J. Chromatogr.* **1988**, *445* (1), 285–289.
- (38) Prud'homme, R. K.; Aksay, I. A.; Adamson, D.; Abdala, A. *Thermally exfoliated graphite oxide and polymer nanocomposites*. US7658901B2, 2010.
- (39) Staudenmaier, L. *Ber. Dtsch. Chem. Ges.* **1898**, *31*, 1481–1487.
- (40) de Koning, G. J. M.; van Bilsen, H. M. M.; Lemstra, P. J.; Hazenberg, W.; Witholt, B.; Preusting, H.; van der Galiën, J. G.; Schirmer, A.; Jendrossek, D. *Polymer* **1994**, *35* (10), 2090–2097.
- (41) Nerkar, M.; Ramsay, J.; Ramsay, B.; Kontopoulou, M.; Hutchinson, R. *J. Polym. Environ.* **2013**, *21* (1), 24–29.
- (42) Kokta, B. V.; Valade, J. L.; Hornof, V.; Law, K. N. *Thermochim. Acta* **1976**, *14* (1–2), 71–86.
- (43) Kashiwagi, T.; Du, F.; Douglas, J. F.; Winey, K. I.; Harris, R. H.; Shields, J. R. *Nat. Mater.* **2005**, *4* (12), 928–933.
- (44) Kim, K.; Regan, W.; Geng, B.; Alemán, B.; Kessler, B. M.; Wang, F.; Crommie, M. F.; Zettl, A. *physica status solidi (RRL) – Rapid Research Letters* **2010**, *4* (11), 302–304.
- (45) Wilkie, C. A.; Morgan, A. B. *Fire retardancy of polymeric materials*. CRC Press: Boca Raton, FL, 2010.
- (46) Noda, I.; Green, P. R.; Satkowski, M. M.; Schechtman, L. A. *Biomacromolecules* **2005**, *6* (2), 580–586.
- (47) Pinto, A. M.; Cabral, J.; Tanaka, D. A. P.; Mendes, A. M.; Magalhães, F. D. *Polym. Int.* **2013**, *62* (1), 33–40.
- (48) Lin, G.; Noda, I.; Mark, J. E. In *Graphite, Graphene, and their Polymer Nanocomposites*; Mukhopadhyay, P., Gupta, R. K., Eds. CRC Press: Boca Raton, FL, 2013; pp 423–446.

- (49) Li, Y.; Kröger, M.; Liu, W. K. *Phys. Rev. Lett.* **2012**, *109* (11), 118001.
- (50) Miloaga, D. G.; Hosein, H.-A. A.; Misra, M.; Drzal, L. T. *J. Appl. Polym. Sci.* **2007**, *106* (4), 2548–2558.
- (51) Sridhar, V.; Lee, I.; Chun, H. H.; Park, H. *eXPRESS Polym. Lett.* **2013**, *7* (4), 320–328.
- (52) Bordes, P.; Pollet, E.; Bourbigot, S.; Avérous, L. *Macromol. Chem. Phys.* **2008**, *209* (14), 1473–1484.
- (53) Kazatchkov, I. B.; Hatzikiriakos, S. G.; Bohnet, N.; Goyal, S. K. *Polym. Eng. Sci.* **1999**, *39* (4), 804–815.
- (54) Vermant, J.; Ceccia, S.; Dolgovskij, M.; Maffettone, P.; Macosko, C. J. *Rheol. (1978–present)* **2007**, *51* (3), 429–450.
- (55) McLachlan, D. S.; Sauti, G. *J. Nanomater.* **2007**, *2007*, 30389.
- (56) Liu, X.; Metcalf, T. H.; Robinson, J. T.; Houston, B. H.; Scarpa, F. *Nano Lett.* **2012**, *12* (2), 1013–1017.
- (57) Harris, A. M.; Lee, E. C. *J. Appl. Polym. Sci.* **2008**, *107* (4), 2246–2255.
- (58) Crist, B.; Fisher, C. J.; Howard, P. R. *Macromolecules* **1989**, *22* (4), 1709–1718.
- (59) Sedighiamiri, A.; Van Erp, T. B.; Peters, G. W. M.; Govaert, L. E.; van Dommelen, J. A. W. *J. Polym. Sci., Part B: Polym. Phys.* **2010**, *48* (20), 2173–2184.
- (60) Halpin, J.; Kardos, J. *J. Appl. Phys.* **1972**, *43* (5), 2235–2241.
- (61) Du, F.; Scogna, R. C.; Zhou, W.; Brand, S.; Fischer, J. E.; Winey, K. I. *Macromolecules* **2004**, *37* (24), 9048–9055.
- (62) Ren, J.; Silva, A. S.; Krishnamoorti, R. *Macromolecules* **2000**, *33* (10), 3739–3746.
- (63) Celzard, A.; McRae, E.; Deleuze, C.; Dufort, M.; Furdin, G.; Marêché, J. F. *Phys. Rev. B: Condens. Matter Mater. Phys.* **1996**, *53* (10), 6209–6214.
- (64) Lu, C.; Mai, Y.-W. *Phys. Rev. Lett.* **2005**, *95* (8), 088303.
- (65) Halpin, J. C.; Kardos, J. L. *Polym. Eng. Sci.* **1976**, *16* (5), 344–352.
- (66) Mori, T.; Tanaka, K. *Acta Metall.* **1973**, *21* (5), 571–574.
- (67) Lu, P.; Leong, Y. W.; Pallathadka, P. K.; He, C. B. *Int. J. Eng. Sci.* **2013**, *73* (0), 33–55.
- (68) Kim, H.; Kobayashi, S.; AbdurRahim, M. A.; Zhang, M. J.; Khusainova, A.; Hillmyer, M. A.; Abdala, A. A.; Macosko, C. W. *Polymer* **2011**, *52* (8), 1837–1846.
- (69) Kim, I.-H.; Jeong, Y. G. *J. Polym. Sci., Part B: Polym. Phys.* **2010**, *48* (8), 850–858.
- (70) Zhang, J.; Qiu, Z. *Ind. Eng. Chem. Res.* **2011**, *50* (24), 13885–13891.
- (71) Kai, W.; Hirota, Y.; Hua, L.; Inoue, Y. *J. Appl. Polym. Sci.* **2008**, *107* (3), 1395–1400.
- (72) Park, J. J.; Yu, E. J.; Lee, W.-K.; Ha, C.-S. *Polym. Adv. Technol.* **2013**, *25* (1), 48–54.
- (73) Yoon, O.; Sohn, I.; Kim, D.; Lee, N.-E. *Macromol. Res.* **2012**, *20* (8), 789–794.
- (74) Li, J.; Kim, J.-K.; Lung Sham, M. *Scripta Mater.* **2005**, *53* (2), 235–240.
- (75) Burnett, T. L.; Yakimova, R.; Kazakova, O. *J. Appl. Phys.* **2012**, *112* (5), 054308–7.
- (76) Schniepp, H. C.; Li, J.-L.; McAllister, M. J.; Sai, H.; Herrera-Alonso, M.; Adamson, D. H.; Prud'homme, R. K.; Car, R.; Saville, D. A.; Aksay, I. A. *J. Phys. Chem. B* **2006**, *110* (17), 8535–8539.
- (77) Celzard, A.; Marêché, J. F.; Furdin, G. *Carbon* **2002**, *40* (14), 2713–2718.
- (78) Chen, G.; Weng, W.; Wu, D.; Wu, C.; Lu, J.; Wang, P.; Chen, X. *Carbon* **2004**, *42* (4), 753–759.
- (79) Celzard, A.; Marêché, J. F.; Furdin, G.; Puricelli, S. *J. Phys. D: Appl. Phys.* **2000**, *33* (23), 3094.
- (80) Zhang, X.; Lin, G.; Abou-Hussein, R.; Allen, W. M.; Noda, I.; Mark, J. E. *J. Macromol. Sci., Part A: Pure Appl. Chem.* **2008**, *45* (6), 431–439.
- (81) Sridhar, V.; Jeon, J.-H.; Oh, I.-K. *Carbon* **2010**, *48* (10), 2953–2957.
- (82) Szatkowski, C.XG Sciences, Inc.: Lansing, MI. Personal communication, 2013.
- (83) Stankovich, S.; Dikin, D. A.; Piner, R. D.; Kohlhaas, K. A.; Kleinhammes, A.; Jia, Y.; Wu, Y.; Nguyen, S. T.; Ruoff, R. S. *Carbon* **2007**, *45* (7), 1558–1565.
- (84) Botas, C.; Pérez-Mas, A. M.; Álvarez, P.; Santamaría, R.; Granda, M.; Blanco, C.; Menéndez, R. *Carbon* **2013**, *63*, 576–578.
- (85) Paredes, J. I.; Villar-Rodil, S.; Martínez-Alonso, A.; Tascón, J. M. D. *Langmuir* **2008**, *24* (19), 10560–10564.
- (86) Bordes, C.; Fréville, V.; Ruffin, E.; Marote, P.; Gauvrit, J. Y.; Briançon, S.; Lantéri, P. *Int. J. Pharm.* **2010**, *383* (1–2), 236–243.
- (87) Lu, W.; Ness, J. E.; Xie, W.; Zhang, X.; Minshull, J.; Gross, R. A. *J. Am. Chem. Soc.* **2010**, *132* (43), 15451–15455.